JOURNAL OF CATALYSIS **166,** 75–88 (1997)
ARTICLE NO. CA971470

An X-Ray Absorption Spectroscopy Determination of the Morphology of Palladium Particles in K L-Zeolite

Paul V. Menacherry, Marcos Fernández-García, and Gary L. Haller

Department of Chemical Engineering, Yale University, 9 Hillhouse Avenue, New Haven, Connecticut 06520

Received January 18, 1996; revised September 26, 1996; accepted September 30, 1996

Particle morphologies for 2 and 3 wt% Pd/K L-zeolite have been determined using X-ray absorption spectroscopy (XAS). X-ray absorption near edge structure–temperature programmed reduction (XANES-TPR) was used to check for the presence of unreduced palladium cations in the locked cages after reduction. A series of calculations were performed to determine coordination numbers for the first three coordination shells for different ideal particle morphologies (spherical, hemispherical, cylindrical, and disc-like). The X-ray absorption fine structure (XAFS) results suggest the formation of ~10 and 16 atom disc-like particles, for 2 and 3 wt% Pd/K L-zeolite, respectively. The lattice expansion for the 3 wt% Pd/K L-zeolite is consistent with chemisorption and TPD of hydrogen and indicates a bulk hydride formation. The effects of morphology and metal support interaction on neopentane conversion over these catalysts are briefly discussed.

INTRODUCTION

It has long been recognized that high quality XAFS data (high signal to noise ratio in an extended range in k-space) can be used to obtain information about the geometrical structure of supported metal catalysts. The XAFS analysis can be used to determine the coordination numbers for the successive coordination shells of the metal. Since the relative contribution of each shell will depend on both the size and the shape of the particle, these results can be used to determine the morphology of the supported particles. The early work of Greegor and Lytle (1) recognized this possibility, and the authors have reported the results of model calculations to study the change in coordination numbers with particle size, for different particle morphologies. Lagarde *et al.* (2) reported the first morphological analysis using the first four coordination shells of a 1 wt% Pt/alumina catalyst; the coordination numbers obtained were claimed to be consistent with an average metal cluster of 13 atoms. Using this technique, both hemispherical (3) and epitaxial raft-like (4) particles have been observed for supported metal catalysts. The application of XAFS to the characterization of supported metal catalysts has been previously reviewed in the literature (5, 6).

The application of XAFS to determine the geometrical structure of supported metal catalyst is especially sensitive to small metal clusters (<30 atoms) because of dramatic changes in the coordination numbers with particle morphology and is therefore well suited to study metal particles in zeolites. Another distinct advantage is that, because of the geometrical constraints imposed by the zeolite structure, a highly unimodal distribution is expected for well prepared catalysts, which facilitates the interpretation of the XAFS results in terms of particle morphology. For example, Vaarkamp *et al.* have reported the formation of very small (~5 atom) clusters for 1.2 wt% platinum supported on L-zeolites (7, 8).

In the present study, XAFS has been used to characterize palladium supported on K L-zeolite. This is part of ongoing work in our laboratory to study metal-support interactions in zeolite supported platinum and palladium catalysts. Particle morphology can play an important role, especially in structure sensitive reactions. The superior properties of platinum supported on L-zeolite for *n*-hexane aromatization has been recently ascribed to the ability of the L-zeolite to stabilize very small platinum clusters which are more resistant to deactivation than platinum on other supports (9, 10). Higher activation energies are observed for neopentane conversion over palladium supported on L-zeolite (11, 12), compared to palladium supported on Y-zeolites (13), silica (14), and alumina (15). Karpiński *et al.* (11) proposed that the increase in activation energies was due to single file diffusion in the L-zeolite pores. However, platinum supported on L-zeolite (12, 16) does not exhibit these higher activation energies. Also, recent results from our laboratory indicate that neopentane conversion over these catalysts is not intracrystalline diffusion controlled. In the present study, we report the results of the XAFS determination of the morphology of the palladium particles supported in K L-zeolite and discuss the effect of morphology/metal–support interaction for neopentane conversion over these catalysts. While XANES study is not the main issue here, it was important to determine if any unreduced Pd^{2+} ions were present after reduction. Any Pd^{2+} present in the locked sites after reduction, e.g., in

0021-9517/97 $25.00

the cancrinite cages, would have a very significant interaction with the lattice oxygen of the zeolite and could account for the large metal–interface contributions observed in the XAFS. Therefore, we have used XANES-TPR to demonstrate that essentially all of the Pd has been reduced to the metal after the reduction step.

EXPERIMENTAL

Catalyst Preparation

The K L-zeolite, obtained from TOSOH (Japan), was used as received. Two Pd/K L-zeolite catalysts (2 and 3 wt% palladium) were prepared by ion-exchange, using tetra amine palladium nitrate as precursor. Portions of the support were slurried in 200 ml/(g of support) deionized water and solutions of the precursor in 100 ml of deionized water were added dropwise over 2 h. The ion-exchange was carried out for 24 h. The samples were subsequently filtered using a Büchner funnel and dried at 140°C for 18 h. They were then calcined at 300°C for 2 h (temperature ramp 2°C/min in 600 ml/g of catalyst × min of oxygen), cooled to room temperature (in 400 ml/g of catalyst per min of helium), and reduced at 400°C (temperature ramp 2°C/min in 400 ml/g of catalyst per min of hydrogen). The samples were then passivated in air and stored.

Chemisorption

Hydrogen chemisorption experiments were performed in a conventional static adsorption apparatus (17). Portions of catalyst were rereduced at 400°C (temperature ramp 5°C/min in 400 ml/min of hydrogen) for 30 min. The hydrogen uptake was measured for equilibrium pressures in the range 20 to 150 Torr. Table 1 reports the hydrogen uptake (H/M) extrapolated to zero pressure.

TPD of Hydrogen

Temperature programmed desorption (TPD) of hydrogen was carried out in a packed bed configuration using 7 mm id Pyrex tube reactors. The catalyst bed consisted of 100 mg of catalyst diluted in 50 mg of α-alumina. The hydrogen, carrier nitrogen, and reference nitrogen gas flows were controlled using mass flow controllers. Nitrogen was purified upstream of the catalyst bed using an Oxiclear purifying trap (Labclear) and an OMI-2 indicating purifier trap (Supelco, Inc.). Hydrogen was purified upstream of the catalyst bed using an Oxiclear purifying trap and a liquid nitrogen trap. The effluent from the catalyst bed was passed through a dry ice acetone trap before entering the TCD. The samples were rereduced at 400°C (temperature ramp 5°C/min) and then cooled to room temperature in a flow of 10 ml/min of hydrogen and 30 ml/min nitrogen. The hydrogen flow was then switched off, and the reactor purged in the nitrogen (carrier) flow until a stable baseline was reached in the TCD (~1 h). The samples were then subject to a temperature ramp of 6°C/min, and the desorption of hydrogen was monitored using the TCD.

TABLE 1

Hydrogen Chemisorption and TPD Results

Catalyst	H/M (chemisorption)	H/M (TPD of hydrogen)
2 wt% Pd/K L-zeolite	0.58	0.49
3 wt% Pd/K L-zeolite	0.72	0.34

XAFS

X-ray absorption fine structure measurements were performed at the F-2 Wiggler line at the Cornell High Energy Synchrotron Source (CHESS) facility. The monochromator used was a Si(311) double crystal monochromator, detuned to 50% to minimize harmonic contamination. Measurements were performed in the transmission mode, using flowing argon ionization chambers. Samples were pressed in self-supporting wafers (~0.7 absorbance) and placed in a controlled atmosphere cell described elsewhere (17). X-ray absorption spectra were recorded after rereduction at 400°C for 30 min (using a temperature ramp of 5°C/min in 5% H_2/He flow) and cooling to 100 K.

Data reduction of the XAFS raw data was made following standard procedures (18). Background subtraction was performed using smoothing spline/multiple averaging routines, and energy independent normalization was carried out using the postedge atomic contribution at 44 eV from the edge, a node in the XAFS region. Data for phase shift and backscattering amplitude functions were obtained from XAFS measurements of reference compounds. Palladium foil and a 5 wt% Pd/SiO_2 catalyst were used as references for Pd–Pd contributions. The 5 wt% Pd/SiO_2 (first shell coordination number 8.8) was included as a reference to study the possible effect of hydride formation in the XAFS analysis. Palladium oxide (PdO) was the reference compound used for Pd–O contributions. Parameters characterizing high-Z (Pd) and low-Z (O) scatterers were determined by multiple shell fitting in k-space with optimization in r-space using both k^3 and k^1 weighting. The different backscatterers were identified using the difference file technique with phase and amplitude-corrected Fourier transforms (19).

XANES-TPR

XANES measurements were performed at line X23A2 of NSLS (Brookhaven National Laboratory). The monochromator used was a Si(311) double crystal monochromator. Detuning was not performed during the experiments as the source has negligible flux at the third harmonic.

The estimated resolution of the monochromator ($\Delta E/E_0 \sim 3 \times 10^{-5}$) at the Pd K-edge, ~1.0 eV, is sufficient to ensure that the XANES spectrum resolution is dominated by core-hole lifetime broadening. Transmission experiments were carried out using flowing argon ionization chambers. Energy calibration was performed by simultaneously measuring a Pd foil between the second and third ionization chambers. Self-supporting wafers (absorbance ~0.4) were placed in the XAS cell. The samples were first purged for 30 min in nitrogen to obtain the starting point and then subjected to a 30-min H_2 treatment at room temperature, followed by a temperature ramp to 400°C (5°C/min) under hydrogen. This was monitored by XANES spectroscopy.

Factor analysis was used to extract chemical information from the XANES. Principal component factor analysis assumes that a variable—the absorbance, in a set of XANES spectra—can be modeled as a linear sum of uncorrelated components known as factors or eigenvalues (20). To determine which factors correspond to signal and which to noise or low frequency background subtraction errors, an *F* test of the variance associated with a k factor and the summed variance associated with the pool of noise eigenvalues is performed. A k factor is accepted as a principal component factor, associated with the signal, when the percentage of significance level of the *F* test (%SL) is lower than a test level that previous studies recommend be fixed at 5% (21, 22). To help in deciding the number of principal components, the ratio of reduced eigenvalues ($R(r)$) will also be used (22). Once the number of principal components is fixed, to transform these principal components into meaningful XANES spectra, a rotation of the concentration profiles, i.e., the amount of each chemical species along the reduction coordinate, is performed using the varimax method followed by iterative transformation factor analysis (23). The rotation matrix obtained in this way is then used to generate the XANES spectra corresponding to pure Pd species (21).

TABLE 2

XAFS Results for References and Catalysts

Sample	Fit region (Å)	Reference used	Fitting parameters			
			N	*R* (Å)	$\Delta\sigma^2$ (Å $\times 10^4$)	ΔE_0 (eV)
Pd foil						
Pd–Pd 1st shell	4.1–15.6	Pd foil	12.0	2.750	0	0.0
Pd–Pd 2nd shell	4.1–15.6	Pd foil	6.0	3.954	0	9.1
Pd–Pd 3rd shell	4.1–15.6	Pd foil	24.0	4.829	0	−0.7
5 wt% Pd/SiO_2						
Pd–Pd 1st shell	3.9–15.3	Pd foil	8.83	2.798	11	−1.0
Pd–Pd 2nd shell	3.9–15.3	Pd foil	4.34	4.043	11	7.6
Pd–Pd 3rd shell	3.9–15.3	Pd foil	11.56	4.904	11	−2.7
2.0 wt% Pd/KL						
Pd–Pd 1st shell	4.1–14.9	Pd foil	3.37	2.770	33	4.7
Pd–Pd 2nd shell	4.1–14.9	Pd foil	0.48	4.043	33	21.6
Pd–Pd 3rd shell	4.1–14.9	Pd foil	1.76	4.901	33	4.3
Pd–O 1st shell	3.9–9.2	PdO	0.31	2.322	10	13.5
Pd–O 2nd shell	3.9–9.2	PdO	8.09	3.153	180	11.2
2.0 wt% Pd/KL						
Pd–Pd 1st shell	4.1–14.9	Pd/SiO_2	3.42	2.765	22	4.1
Pd–Pd 2nd shell	4.1–14.9	Pd/SiO_2	0.45	4.039	22	21.1
Pd–Pd 3rd shell	4.1–14.9	Pd/SiO_2	1.77	4.898	22	4.5
Pd–O 1st shell	3.9–9.2	PdO	0.29	2.286	10	14.0
Pd–O 2nd shell	3.9–9.2	PdO	4.30	3.129	121	9.3
3.0 wt% Pd/KL						
Pd–Pd 1st shell	4.1–15.4	Pd foil	4.41	2.796	26	6.5
Pd–Pd 2nd shell	4.1–15.4	Pd foil	1.36	4.049	26	13.7
Pd–Pd 3rd shell	4.1–15.4	Pd foil	4.42	4.911	26	1.8
Pd–O 1st shell	3.9–9.2	PdO	0.48	2.316	10	11.2
Pd–O 2nd shell	3.9–9.2	PdO	11.04	3.194	151	12.6
3.0 wt% Pd/KL						
Pd–Pd 1st shell	4.1–15.4	Pd/SiO_2	4.40	2.794	15	6.6
Pd–Pd 2nd shell	4.1–15.4	Pd/SiO_2	1.31	4.034	15	11.1
Pd–Pd 3rd shell	4.1–15.4	Pd/SiO_2	4.48	4.910	15	2.4
Pd–O 1st shell	3.9–9.2	PdO	0.40	2.285	10	12.7
Pd–O 2nd shell	3.9–9.2	PdO	8.18	3.184	130	10.9

Model Calculations for Ideal Particle Geometries

In order to extract particle morphology information from the XAFS results reported in Table 2, we have performed a series of calculations to determine coordination numbers for the first three coordination shells, for different ideal morphologies. Because we are interested in metal particles inside of the zeolite pores, we have focused on the analysis of small particles (less than 40 atoms). In this way, we have extended previous studies (1) to smaller particles. During these calculations the atoms are always placed at fcc lattice positions. Spherical, hemispherical, cylindrical, and disc-like (with 111, 110, and 100 orientations) morphologies were considered and different sized particles were generated by successively including the allowable atoms at the next nearest distance. Spherical and hemispherical particles were calculated with two different origins, one located at an atomic position and the other located midway between two adjacent atoms. Cigar-like structures were modeled by cylinders of 5.6 Å maximum diameter with (111)-orientation. One and two layer discs with (111) orientation were calculated with three different origins, generating particles with D_{6h} (or subgroup) symmetries. For 110 oriented discs, three different origins were used, generating particles with D_{4h} (or subgroup) symmetries. For 100 oriented discs, two origins were used, generating particles with D_{4h} (or subgroup) symmetries. These calculations are summarized in Fig. 1. Note that the single layer disk is easily distinguished from the other morphologies by the lower first and third shell coordination numbers and the absence of the second shell, while the two layer disk has the largest third shell coordination number to second shell coordination number

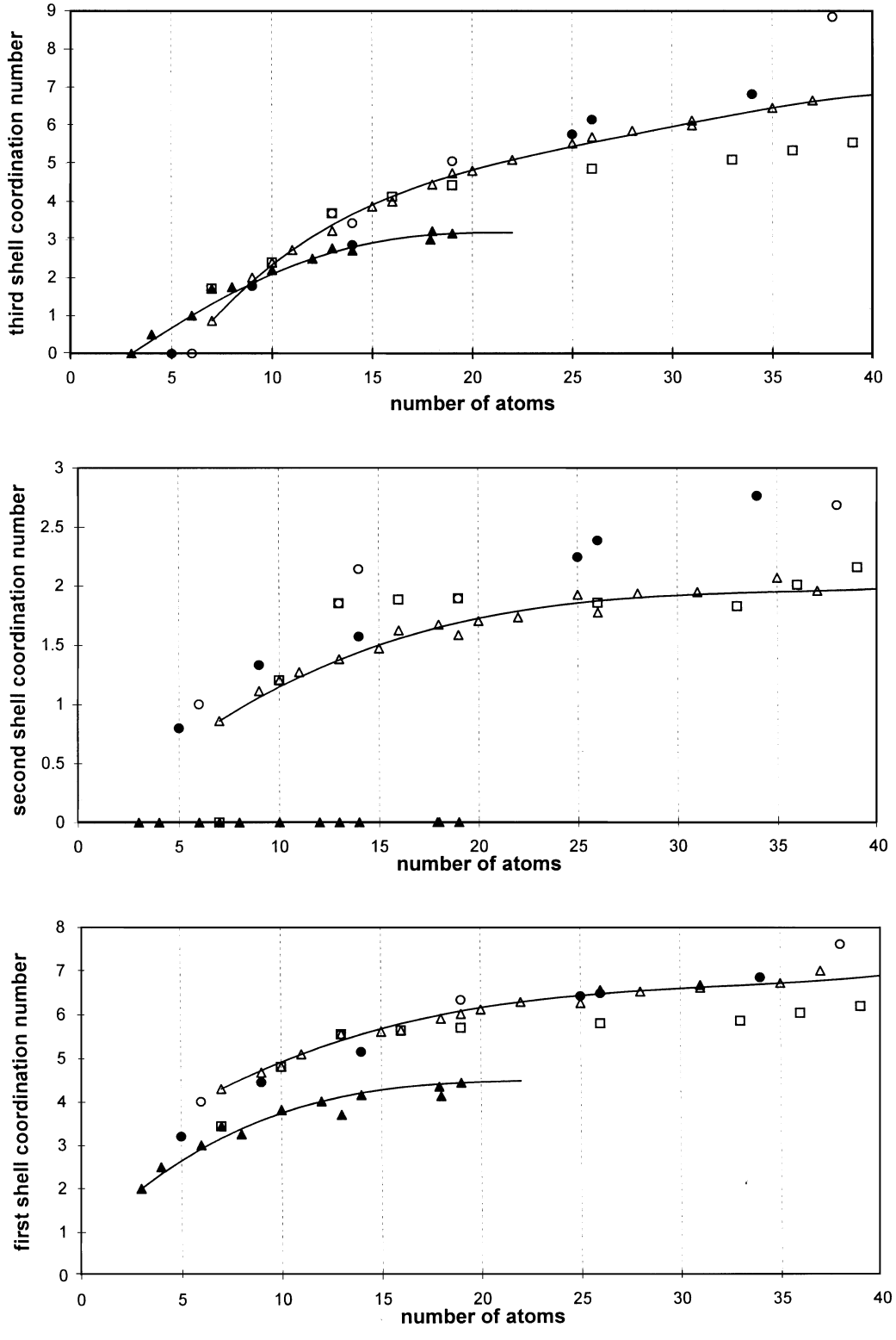

FIG. 1. Coordination numbers vs number of atoms for different particle morphologies. ○, Sphere; ●, hemisphere; □, cylinder; ▲, (111) one-layer disc; △, (111) two-layer disc.

of all the other morphologies studied. These observations guided us in the selection of particle morphologies based on the XAFS results.

RESULTS

Chemisorption/TPD of Hydrogen

The results of the chemisorption and TPD of hydrogen are reported in Table 1. It is observed that for the 2 wt% Pd/K L-zeolite, the H/M values for chemisorption and TPD of hydrogen are quite close, while for the 3 wt% Pd/K L-zeolite, the H/M values for chemisorption is roughly twice that for TPD of hydrogen. This indicates a possible hydride formation (i.e., presence of weakly held subsurface hydrogen) for the 3 wt% Pd/K L-zeolite, which is in agreement with the increased Pd–Pd distances for this sample, compared to the 2 wt% Pd/K L-zeolite and the palladium foil, as determined by XAFS (see below).

XAFS

The results of the XAFS analysis are reported in Table 2. The 5 wt% Pd/SiO_2 has rather large particles (first shell coordination about 9) and an expanded Pd–Pd internuclear distance compared to the foil, consistent with Pd hydride formation. The phase and amplitude functions extracted from the Pd foil and Pd/SiO_2 references are shown in Fig. 2. These were the phase and amplitude functions used in the fits of the 2 and 3 wt% Pd/K L-zeolite catalysts. Note that in the case of the 2 and 3 wt% Pd/K L-zeolite catalysts there are two independent fits using both the Pd foil reference and the Pd hydride reference in combination with the PdO reference. The χ functions are shown in Fig. 3, and the comparisons between normalized Fourier transforms of the sample and palladium foil are shown in Figs. 4a and 4b, for the 2 and 3 wt% Pd/K L-zeolite, respectively. The high signal to noise ratio allowed the use of an extended range (up to ~16 $Å^{-1}$), even for the 2 wt% Pd/K L-zeolite. The comparison between normalized Fourier transforms indicates the presence of two metal–zeolite wall interface contributions, one at ~1.8 Å and the other at ~2.8 Å (uncorrected distances). In contrast, in the comparison of the normalized Fourier transform of 5 wt% Pd/SiO_2 with palladium foil (Fig. 4c), it is seen that the 5 wt% Pd/SiO_2 reference shows negligible metal–support contribution, which suggests that the interface contributions observed in the 2 and 3 wt% Pd/K L-zeolites are real and not a hydride related artifact. The signals were Fourier transformed in the range 2.76–16.4 $Å^{-1}$ (15.8 $Å^{-1}$ for the 2 wt% Pd/K L-zeolite) in k-space. The inverse Fourier transforms were extracted in the range 1.79–5.06 Å. The fits were performed in the range 3.9–15.4 $Å^{-1}$ in k-space (14.9 $Å^{-1}$ for the 2 wt% Pd/K L-zeolite). The number of free parameters, as calculated from the Nyquist formula (~25), were in excess of the number of parameters used in the fits (i.e., 20). We found that the introduction of the Pd–O contribution resulted in ~10% of change in the coordination numbers of the Pd–Pd contributions determined by fitting the k^3 weighted inverse function between 9.3 and 15.4 $Å^{-1}$ (14.9 $Å^{-1}$) in k-space. The Pd–Pd coordination numbers determined using the palladium hydride reference and the Pd hydride reference are almost

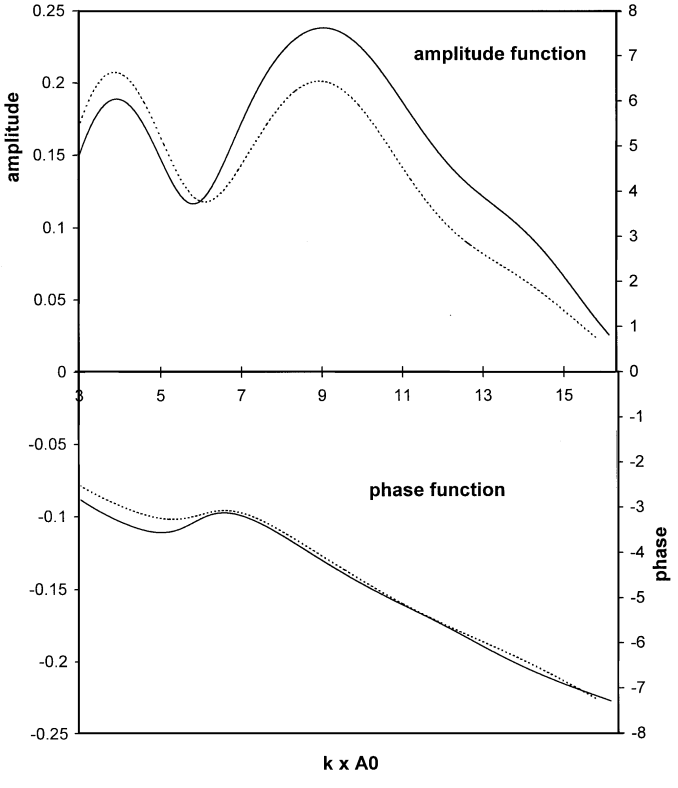

FIG. 2. Phase and amplitude functions for Pd foil and the 5 wt% Pd/SiO_2 references.

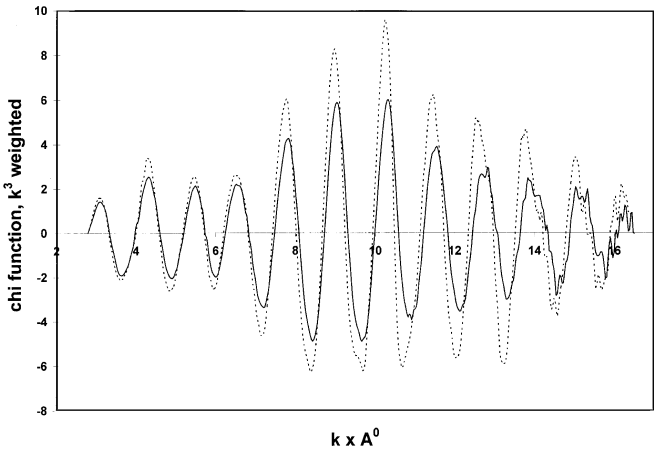

FIG. 3. k^3-Weighted χ functions for the 2 wt% Pd/K L-zeolite (solid line) and 3 wt% Pd/K L-zeolite (dashed line) samples.

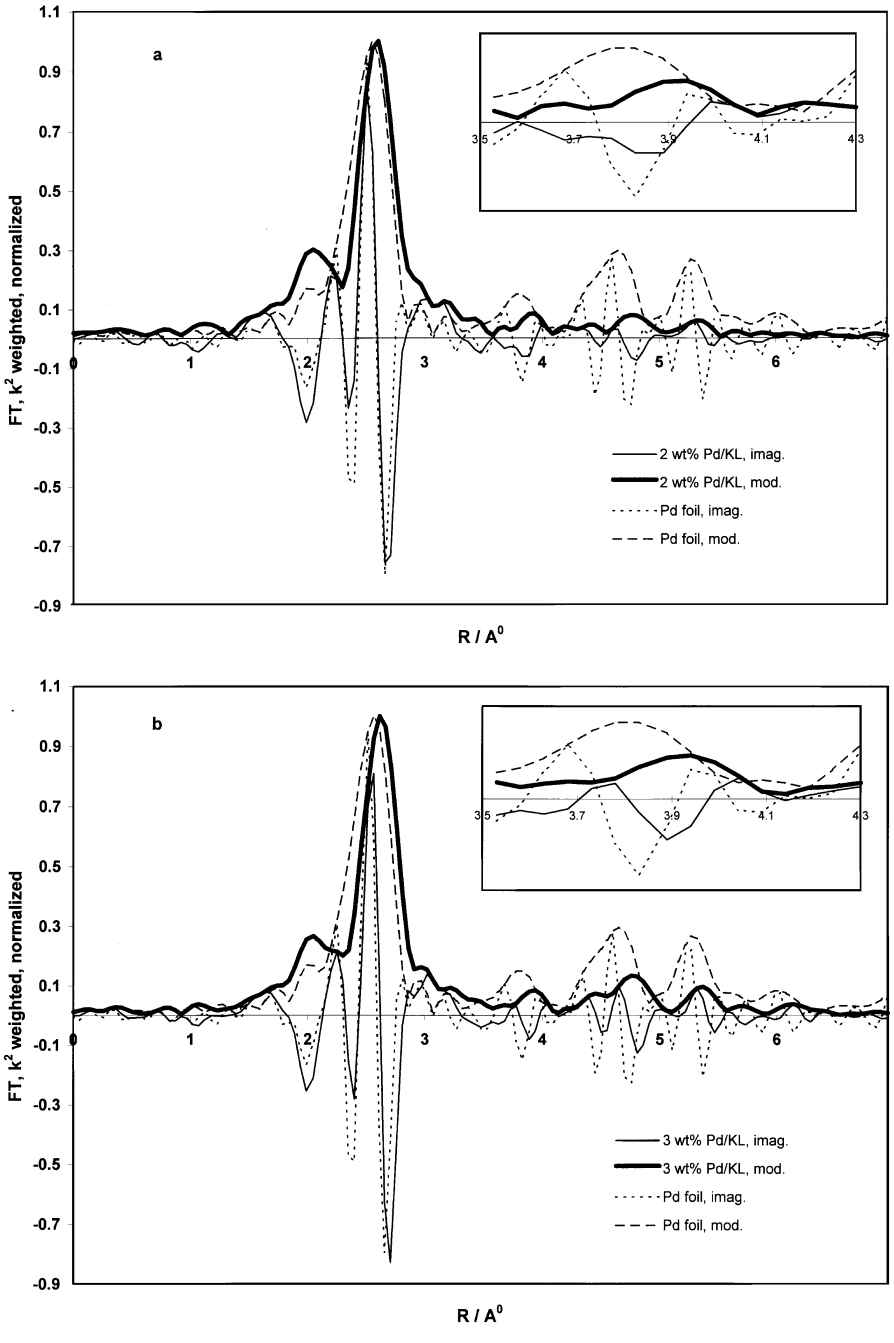

FIG. 4. Comparison of normalized Fourier transforms of 2 and 3 wt% Pd/K L-zeolite and 5 wt% Pd/SiO_2 with Pd foil reference.

identical. This clearly shows that the EXAFS analysis is not affected by the presence of hydride phases. However, the Pd hydride reference gave slightly better fits in both cases, and therefore we have chosen to show these results in the following figures. The Fourier filtered χ functions and total fits are shown in Fig. 5, comparisons of the k^3 weighted, Pd–Pd phase corrected Fourier transforms of the Fourier filtered χ functions and the fits are shown in Fig. 6, and Fourier transforms of difference files showing the metal–zeolite wall interface contributions to the fits are shown in Fig. 7.

XANES-TPR

The results of XANES-TPR for the 3 wt% Pd/K L-zeolite are shown in Table 3. Both the reduced eigenvalues and the *F* test conclusively show the existence of four principal components. The evolution of the corresponding four pure Pd

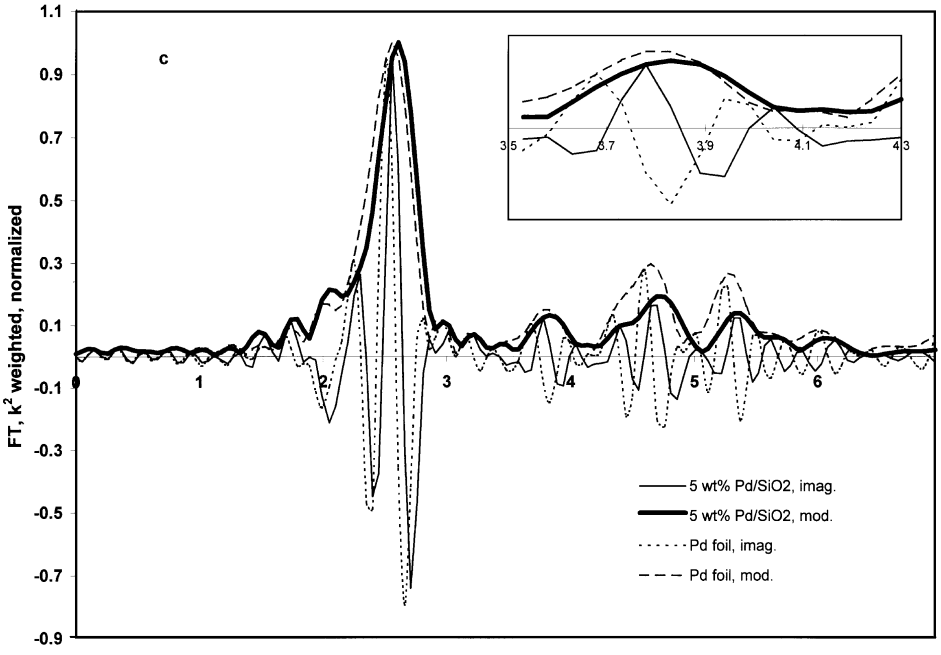

FIG. 4—*Continued*

species are shown in Fig. 8. Two of the species (species 3 and 4) are oxidic species which are consumed during the hydrogen treatment (Fig. 9). Species number 1 presents a maximum concentration at about 50°C and should correspond to a hydride phase (actually an average over the hydride phases formed during the reduction). Only one species remains at the end of the experiment. This species, No. 2 in Fig. 9, corresponds to a metallic Pd. The XANES-TPR results of the 2 wt% Pd/K L-zeolite (not shown for the sake of brevity) indicates the existence of primarily three species. The hydride phase is negligible, in agreement with the TPD and XAFS results previously presented. The three species observed are almost identical to species 2, 3, and 4 of Fig. 9. A complete XANES analysis will be reported elsewhere (24).

TABLE 3

Principal Component Analysis Results for 3 wt% Pd/K L-zeolite

Factor	Eigenvalue	%SL	*R*(*r*)	Variance
1	834.010	0.00	945.00	99.893
2	0.81089	0.00	11.20	0.097
3	0.06586	0.14	4.41	0.008
4	0.01354	0.72	4.45	0.001
5	0.00274	7.78	1.80	0.001
6	0.00135	11.13	3.55	
7	0.00034	37.99	1.02	
8	0.00028	39.96	0.85	
9	0.00028	37.50	1.14	
10	0.00020	43.12	0.97	
11	0.00017	46.85	0.88	
12	0.00014	50.89	0.77	

DISCUSSION

Morphology of Palladium Particles

As seen in Table 2, the second Pd–Pd coordination shell of the 2 wt% Pd/K L-zeolite is only about 10% of that for the 5 wt% Pd/SiO_2 sample and about a third of that for the 3 wt% Pd/K L-zeolite. This difference is less obvious in the normalized Fourier transforms (Fig. 4), but it can be seen that the shape of the imaginary part of the 2 wt% Pd/K L-zeolite sample is significantly different from Pd foil in the region between 3.7 and 4.1 Å (see expanded insert), while both the 3 wt% Pd/K L-zeolite and the 5 wt% Pd/SiO_2 are not. This suggests that this peak in the radial distribution function may be have a large contribution from multiple scattering paths (further discussed below). The near absence of the second coordination shell (coordination number <0.5) suggests a particle morphology resembling a single-layer, (111)-oriented, disc-like structure. The Pd–Pd coordination numbers obtained match very closely those of the 9- and 10-atom particles shown in Fig. 10. Note that the near absence of interstitial positions for the model particles proposed for the 2 wt% Pd/K L-zeolite explains the negligible hydride formation and the significantly less distorted Pd–Pd distances.

The 3 wt% Pd/K L-zeolite sample has first, second, third, and fourth coordination shells corresponding to an expanded fcc lattice (Table 2). The coordination numbers

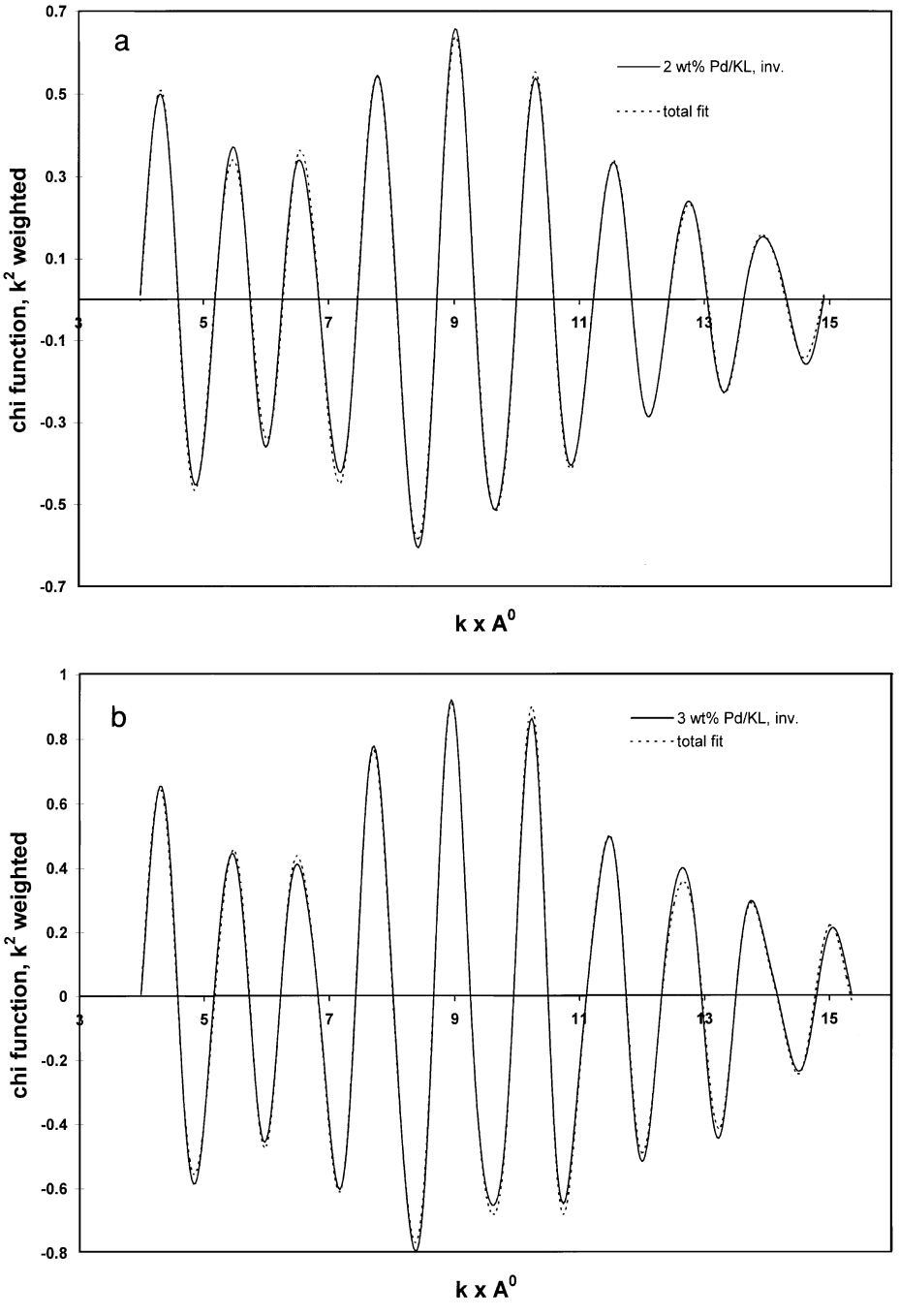

FIG. 5. Comparison of Fourier filtered χ functions with fits.

obtained from the analysis do not fit any of the standard geometries, because of the high third shell to second shell ratio; this ratio (∼3.5) is too high for any of the ideal geometries studied for a first shell coordination number between 4 and 5. A bimodal distribution of particles, in which the high third shell to first shell ratio can come from a fraction of the metal particles outside of the zeolite pores, is not in keeping with the increased Pd–O contribution at ∼3.2 Å compared to the 2 wt% Pd/K L-zeolite. An analysis of the change in coordination numbers with the addition of adatoms to the particles obtained from the model calculations showed that an increase in third shell coordination number, with only moderate increase in first and second shell coordination numbers, can be obtained by the addition of adatoms on both sides of a single-layer (111) disc. Proceeding along this line of thought, we were able to find a 16-atom particle morphology that matched (within ∼10%) the coordination numbers determined from XAFS (see Fig. 10). This particle has

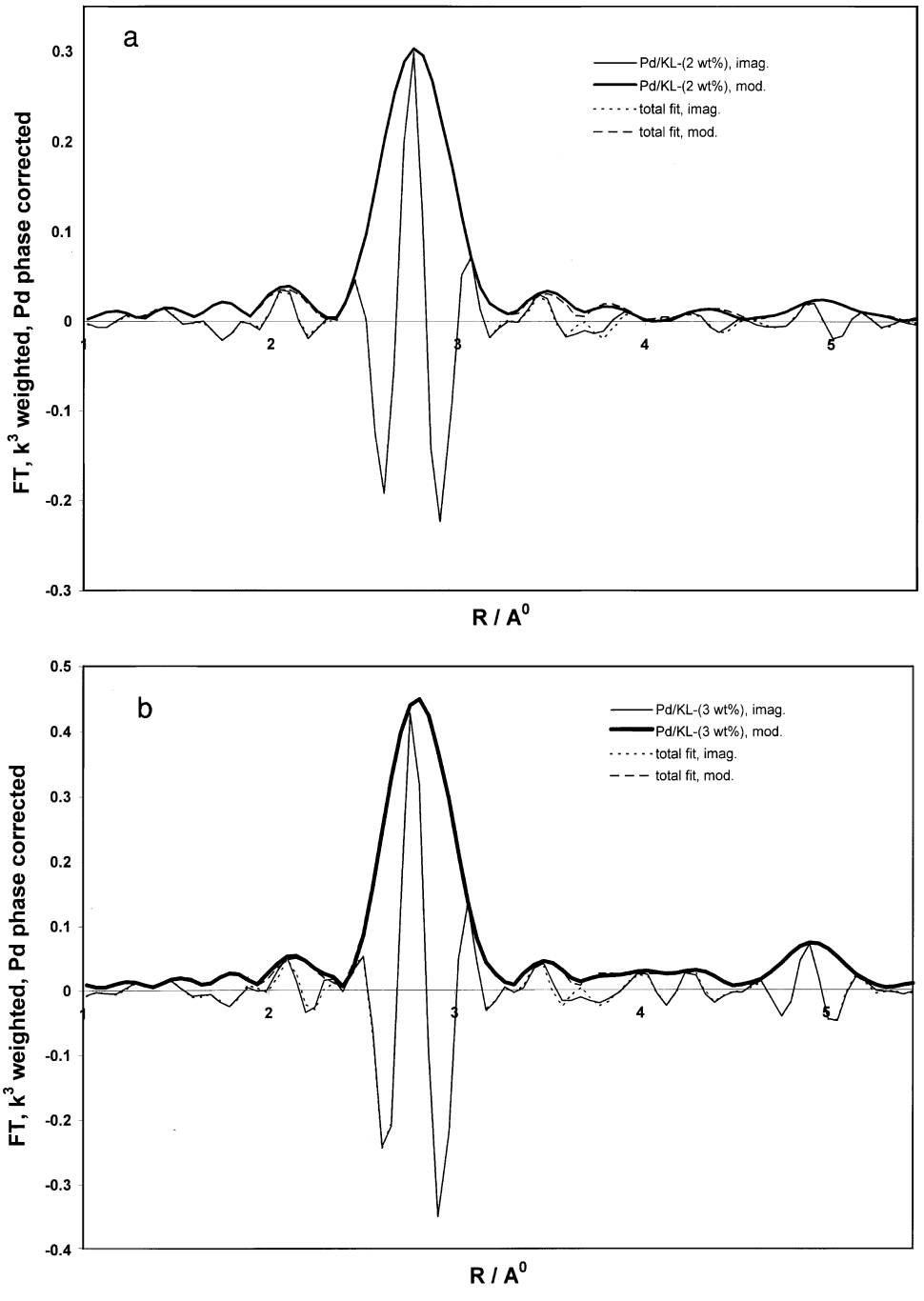

FIG. 6. Comparison of k^3-weighted Fourier transforms (Pd-phase corrected) of the Fourier filtered χ functions with fits.

interstitial sites for hydrogen adsorption and consequently allows the formation of the hydride phase (25), detected by TPD and the expansion of the metal lattice observed by XAFS.

XAFS data can have important contributions from multiple scattering paths. The recent work of Zabinsky *et al.* (26) has extensively discussed the contribution of multiple scattering to XAFS for fcc structures. Although important contributions of multiple scattering were thought to exist at or above the distances of the fourth coordination shell, their calculations show that there can be significant multiple scattering (triangular) paths, at effective path lengths close to the second and third coordination shell distances, for some particle morphologies. Here, one may be concerned whether multiple scattering would significantly affect the coordination numbers determined for the second and third

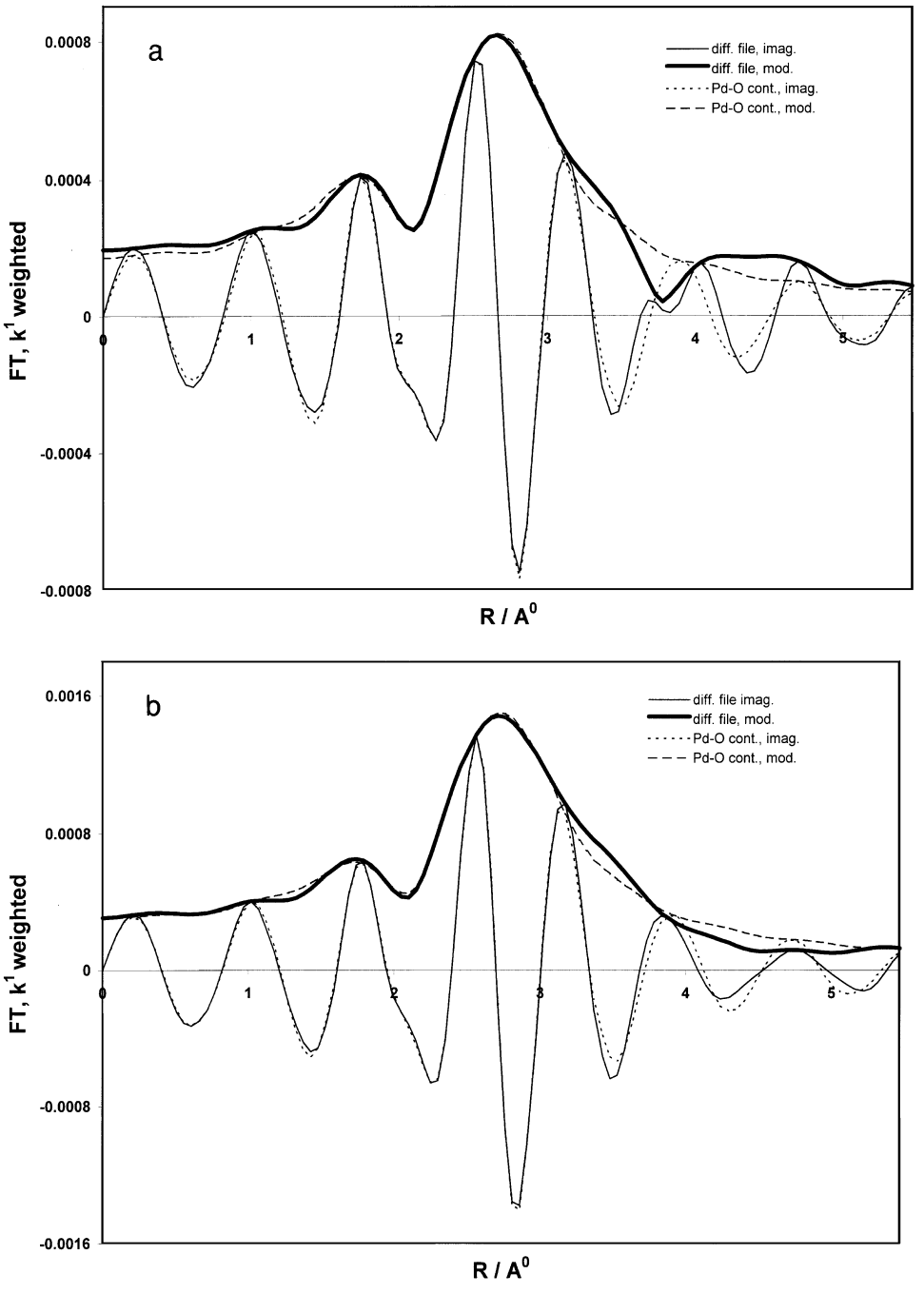

FIG. 7. Comparison of k^1-weighted Fourier transforms of the difference files with the Pd–O contributions calculated using Pd–O phase and amplitude function extracted from PdO reference.

coordination shells. However, from a comparison of the reported degeneracies for the bulk fcc lattice to the average number of paths calculated for the suggested particle morphologies, we have estimated that these multiple scattering paths (path labels 111 and 211, in the notation of Lee and Pendry (27)) would contribute less than 5% to the second and third shells of the 14- and 16-atom particles and the third shell of the 9- and 10-atom particles. However, as mentioned previously, because of the near absence of the second shell for the 2 wt% Pd/K L-zeolite catalyst, this shell can have a significant contribution from the 111 (triangular) multiple scattering path, and this could affect the coordination number determined for the Pd–Pd second shell contribution in this case.

Another interesting point in the XAFS analysis is the existence of large Pd–O contributions at ~2.3 and 3.2 Å

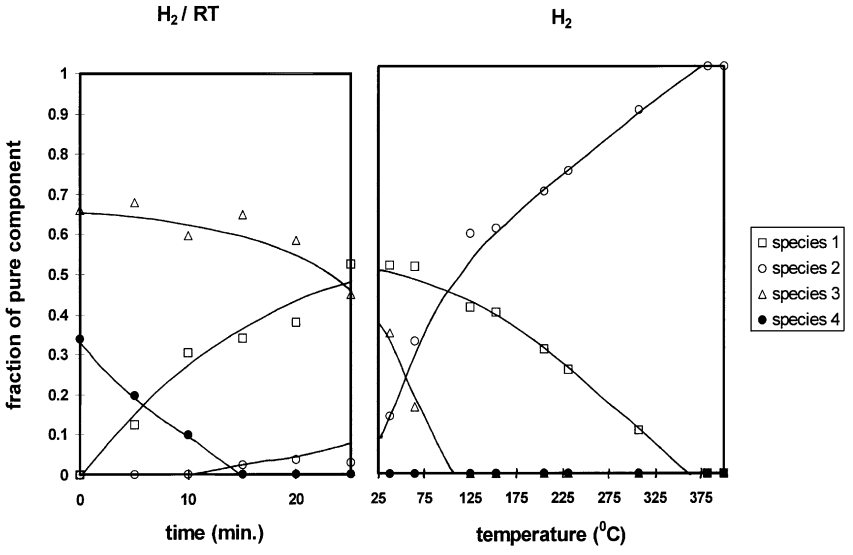

FIG. 8. Factor analysis determined evolution of species for the XANES-TPR of 3 wt% Pd/K L-zeolite.

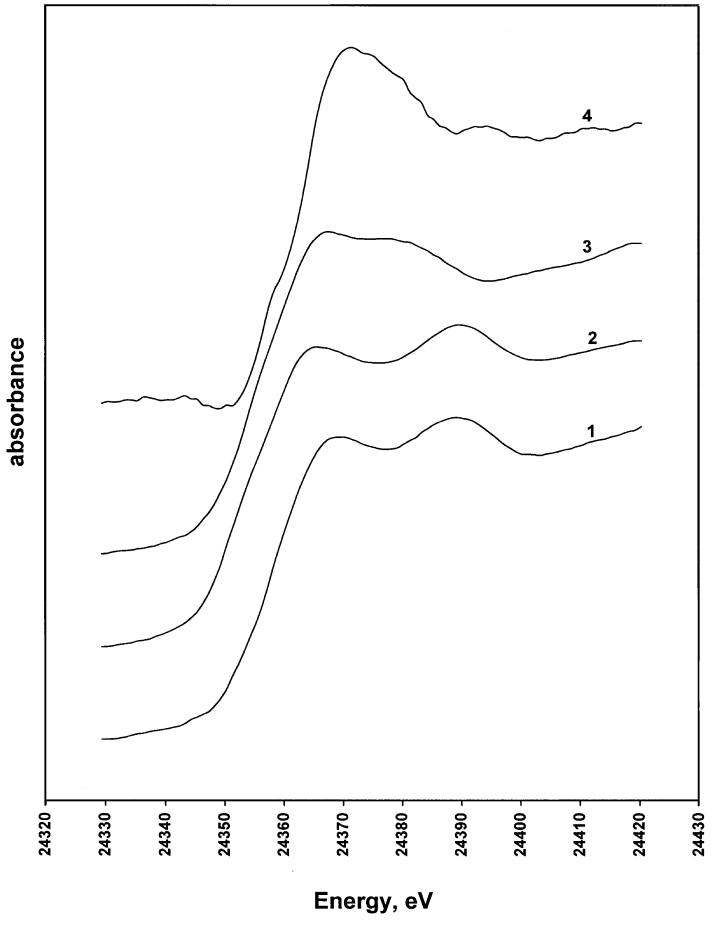

FIG. 9. Identification of species by factor analysis of XANES-TPR data for 3 wt% Pd/K L-zeolite. Species 1 is assigned to the hydride phase, species 2 to metallic Pd, and species 3 and 4 to oxidic Pd phases.

TABLE 4

Palladium–Zeolite Wall Interface Single Scattering Contributions for Metal Particles in the Main Channel of L-zeolite

	Single scattering paths between 2.1 and 2.5 Å				Single scattering paths between 2.5 and 3.75 Å			
	Pd–O contributions		Pd–Si contributions		Pd–O contributions		Pd–Si contributions	
Particle	No.	*d* (Å)	No.	*d* (Å)	No.	*d* (Å)	No.	*d* (Å)
10-Atom particle	3	2.32	0	—	38	3.20	18	3.34
16-Atom particle	6	2.28	2	2.46	40	3.47	18	3.60

Note. d, mean path length.

for both the 2 and the 3 wt% Pd/K L-zeolite. These are significantly larger than metal–support coordination numbers reported previously for metal–oxide (6) and Pt/K L-zeolite (7, 8) systems. Because these contribution may, at least in part, originate from palladium cationsin the locked cages, the rereduction of passivated samples was followed by XANES-TPR. As explained in the results section, no cationic species were detected, and all of the palladium was in the metallic state after rereduction at 400°C. Therefore, no correction has to be made to the coordination numbers obtained by XAFS. Thelarge Pd–O coordination numbers (Table 2) may come from zeolite lattice oxygens surrounding the metal particles. The large Debye–Waller terms used in the fitting for the second Pd–O contribution clearly indicate that this contribution, in fact, represents a series of distances centered around 3.2 Å, rather than a unique distance. To check this hypothesis, we have calculated the number of Pd-zeolite wall interface single scattering paths (out to 3.75 Å) for the suggested metal particles in possible orientations within the main channel of the L-zeolite (shown in Figs. 11 and 12). The results are reported in Table 4. From these calculations it is clear that these high Pd–O contributions can come from the interface. It should be noted that in these orientations the smallest Pd–O distances were always >2.1 Å. Our calculations also show that

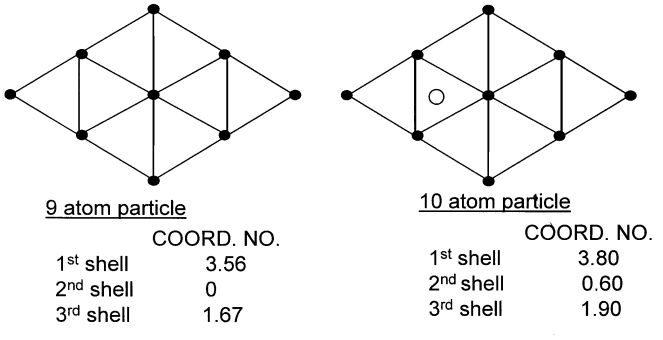

FIG. 10. Schematic representations of the different particle morphologies suggested by the XAFS results. ○, Atoms below the plane of paper; x, atoms above the plane of paper.

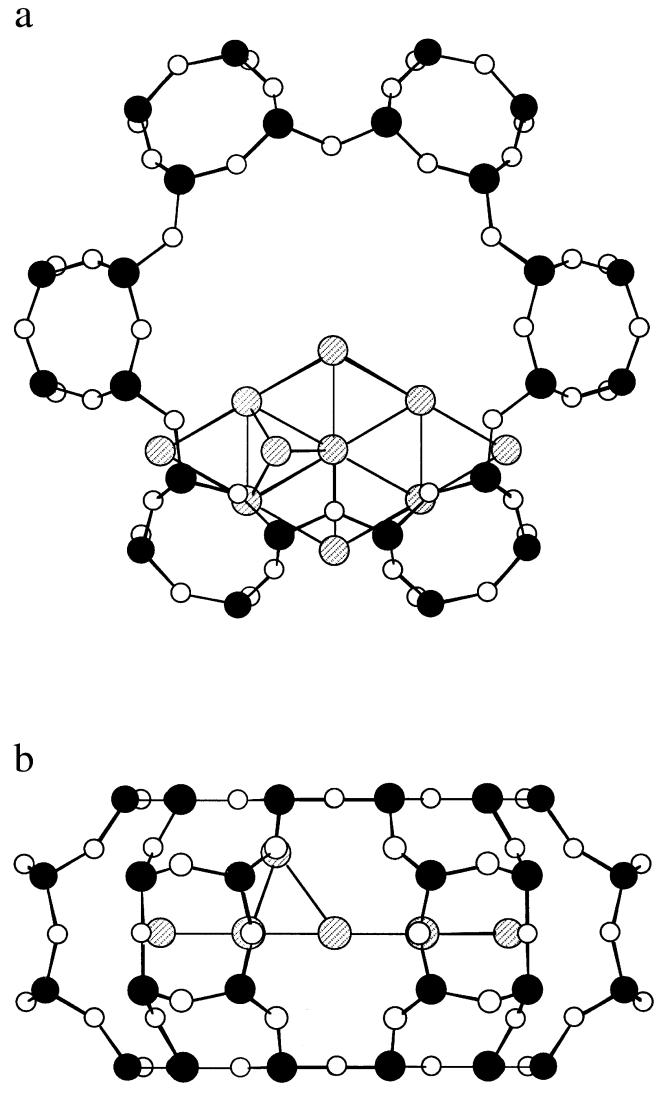

FIG. 11. Ten-atom particle. (a) Viewed along *c*-axis of L-zeolite channel. (b) Viewed perpendicular to *c*-axis of L-zeolite channel.

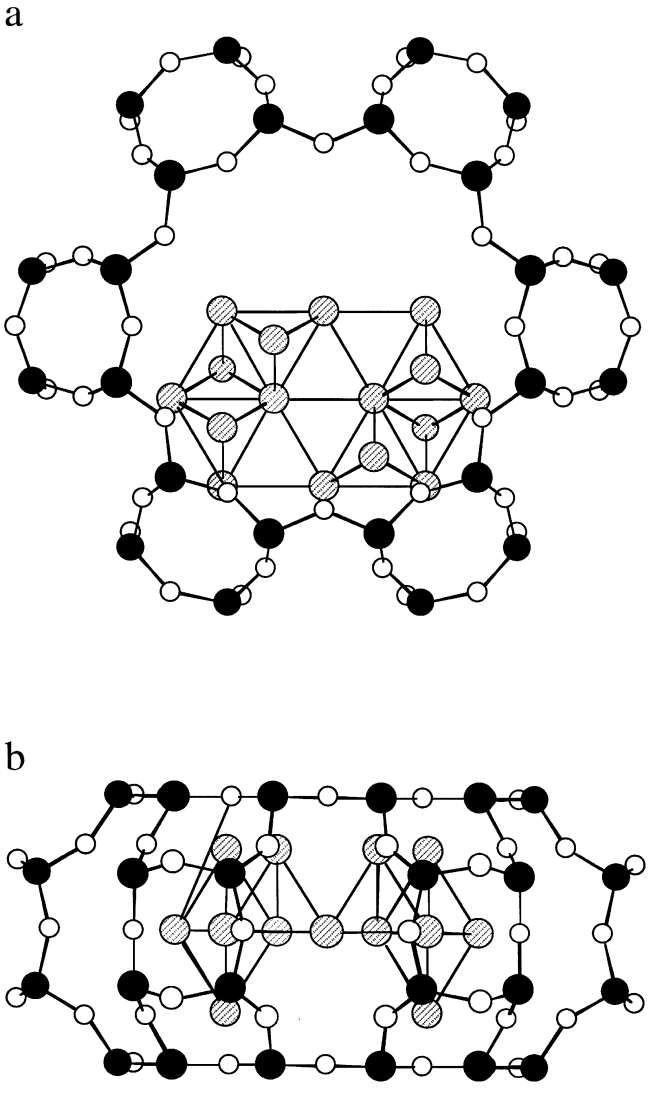

FIG. 12. Sixteen-atom particle. (a) Viewed along *c*-axis of L-zeolite channel. (b) Viewed perpendicular to *c*-axis of L-zeolite channel.

there can also be significant backscattering from Si atoms at these distances. We compared the phase functions of theoretical Pd–Si and Pd–O references (generated using the UWEXAFS package) and found a nearly constant difference in phase of ~3.5 radians. Therefore, using the Pd–O reference to fit the Pd–Si contributions will give approximately correct coordination distances, but larger coordination numbers, because of the smaller scattering amplitude of the oxygen atom compared to the silicon atom. Because what we have is a series of Pd–O and Pd–Si contributions at different distances, it is very difficult to predict the resulting interference phenomenon. In addition to the presence of silicon atom backscatterers, because of the important difference in distances between the Pd–O contributions and the reference used in the XAFS analysis, the possible focusing effect of hydrogen atoms (or protons), and the presence of possible Pd–O–Si multiple scattering paths, the coordination numbers reported for the Pd–O contribution should be regarded as semiquantitative only. It must be reiterated that the positioning of the particles within the main cage of the L-zeolite shown in Figs. 11 and 12 was arbitrary (based on roughly maximizing the Pd–O contribution) and was intended for illustrative purposes only. However, this does enable us to rationalize the high metal–zeolite wall interface contributions observed.

Effect of Morphology on Catalytic Behavior

The peculiar morphology of palladium particles in K L-zeolite may be related to the anomalous catalytic behavior of these catalysts for neopentane conversion. Karpiński *et al.* (11) first reported the higher activation energies for neopentane conversion over palladium supported on L-zeolite. These high activation energies are not observed for palladium supported on Y-zeolite (13) and supports like silica (14) and alumina (15), in which the particles are thought to be spherical or hemispherical. In recent work in our laboratory, these higher activation energies were attributed to a bimolecular reaction pathway for the hydrogenolysis of neopentane, in which the transition state is formed from two adsorbed neopentane molecules (12). The 2 and 3 wt% Pd/K L-zeolite have very similar activation energies and preexponential factors for neopentane conversion (12). We propose that the anomalous behavior of palladium supported on L-zeolite for neopentane conversion (11, 12) may be related to the disc-like morphology of the metal particles formed, which favor a bimolecular reaction pathway for neopentane conversion over these catalysts. Karpiński *et al.* have studied neopentane conversion over (111) oriented Pd films; however, due to complications like poisoning of the catalytic surface during reaction, no clear picture of the effect of the (111) orientation of palladium atoms was observed (28).

CONCLUSION

Coordination numbers for the first three Pd–Pd coordination shells (and for the Pd–zeolite wall interface at ~2.3 and 3.2 Å) were determined for 2 and 3 wt% Pd/K L-zeolite. The coordination numbers for the 2 wt% Pd/K L-zeolite match those of a 9- or 10-atom disc-like particle. The coordination numbers for the 3 wt% Pd/K L-zeolite match those of a 16-atom particle generated by the addition of adatoms to a single layer, (111) disc-like particle. The Pd–Pd coordination numbers and the large Pd–O coordination number indicate that the palladium particles may have a free standing disc-like structure. Therefore, it appears that the morphology of the metal particles formed is dictated by the interaction with the L-zeolite lattice. It has been demonstrated that the large Pd–O coordination numbers obtained for these samples can arise from the L-zeolite

lattice. The peculiar morphology of the palladium particles explains the presence/near absence of the hydride phase for the 3 and 2 wt% Pd/K L-zeolite, respectively, because the latter morphology has a greatly reduced number of interstitial sites needed for hydride formation. The anomalous behavior of palladium supported on L-zeolite for neopentane conversion, compared to palladium supported on Y-zeolite and on supports like silica and alumina, may be related to the peculiar morphology of the metal particles formed.

ACKNOWLEDGMENTS

We thank I. Wu for providing the 5 wt% Pd/SiO_2 reference and H. Wang for help with generating the zeolite matrix and the theoretical references. M.F.G. thanks the "Ministerio de Educacion y Ciencia" of Spain for a Postdoctoral Fellowship. Financial support was provided by the Department of Energy, Office of Basic Energy Sciences. The X-ray absorption experiments were carried out at Cornell High Energy Synchrotron Source (CHESS), Ithaca, and the National Synchrotron Light Source (NSLS), Brookhaven National Laboratory.

REFERENCES

1. Greegor, R. B., and Lytle, F. W., *J. Catal.* **63**, 476 (1980).
2. Lagarde, P., Murata, T., Vlaic, G., Freund, E., Dexpert, H., and Bournonville, J. P., *J. Catal.* **84**, 333 (1983).
3. van Zon, F. B. M., Thesis, Eindhoven University, The Netherlands, 1988.
4. van Zon, F. B. M., Visser, G., and Koningsberger, D. C., *in* "Proceedings, 9th International Congress on Catalysis, Calgary, 1988" (M. J. Phillips and M., Ternan, Eds.), Chem. Institute of Canada, Ottawa, 1988.
5. Conesa, J. C., Esteban, P., Dexpert, H., and Bazin, D., *Stud. Surf. Sci. Catal.* **57**A, 225 (1990).
6. Koningsberger, D. C., and Gates, B. C., *Catal. Lett.* **14**, 271 (1992).
7. Vaarkamp, M., Grondelle, J. V., Miller, J. T., Sajkowski, D. J., Modica, F. S., Lane, G. S., Gates, B. C., and Koningsberger, D. C., *Catal. Lett.* **6**, 369 (1990).
8. Vaarkamp, M., Mojet, B. L., Kappers, M. J., Miller, J. T., and Koningsberger, D. C., *J. Phys. Chem.* **99**, 16067 (1995).
9. Sharma, S. B., Ouraipryvan, P., Nair, H. A., Balaraman, P., Root, T. W., and Dumesic, J. A., *J. Catal.* **150**, 234 (1994).
10. Mielczarski, E., Hong, S. B., Davis, R. J., and Davis, M. E., *J. Catal.* **134**, 359 (1992).
11. Karpiński, Z., Gandhi, S. N., and Sachtler, W. M. H., *J. Catal.* **141**, 337 (1993).
12. Menacherry, P. V., and Haller, G. L., submitted for publication.
13. Homeyer, S. T., Karpiński, Z., and Sachtler, W. M. H., *Recl. Trav. Chim. Pays-Bas* **109**, 81 (1990).
14. Karpiński, Z., Butt, J. B., and Sachtler, W. M. H., *J. Catal.*, 521 (1989).
15. Juszczyk, W., Lomot, D., Karpiński, Z., and Pielaszek, J., *Catal. Lett.* **31**, 37 (1995).
16. Larson, G., and Haller, G. L., *Catal. Today* **15**, 431 (1992).
17. Larson, G., Ph.D. thesis, Yale University, 1993.
18. Lytle, F. W., Sayers, D. E., and Stern, E. A., *Physica* B **158**, 701 (1989).
19. van Zon, J. B. D. A., Koningsberger, D. C., Van't Blink, H. F. J., and Sayers, D. E., *J. Chem. Phys.* **72**, 5742 (1985).
20. Malinowski, E. R., "Factor Analysis in Chemistry," 2nd ed. Wiley, New York, 1991.
21. Fernandez Garcia, M., Alvarez Marquez, C., and Haller, G. L., *J. Phys. Chem.* **99**, 12565 (1995).
22. Fernandez Garcia, M., Alvarez Marquez, C., Rodriguez-Romos, I., Ruiz-Guerrero, A., and Haller, G. L., *J. Phys. Chem.* **99**, 16380 (1995).
23. Gemperline, J. P., *Chem. Inf. Comput. Sci.* **24**, 206 (1984).
24. Fernandez Garcia, M., Menacherry, P. V., and Haller, G. L., unpublished results.
25. McCaulley, J. A., *J. Phys. Chem.* **97**, 10372 (1993).
26. Zabinsky, S. I., Rehr, J. J., Ankudinov, A., Albers, R. C., and Eller, M. J., *Phys. Rev.* B **52**, 2995 (1995).
27. Lee, P. A., and Pendry, J. B., *Phys. Rev.* B **11**, 2795 (1975).
28. Karpiński, Z., Juszczyk, W., and Pielaszek, J., *J. Chem. Soc. Faraday Trans. I* **83**, 1293 (1987).